Joint Cross Well and Single Well Seismic Studies at Lost Hills, California

Gritto R., T.M. Daley, and L.R. Myer

Earth Sciences Division, Center for Computational Seismology, Lawrence Berkeley National Laboratory, Berkeley, CA 94720

ABSTRACT

A series of time-lapse seismic cross well and single well experiments were conducted in a diatomite reservoir to monitor the injection of CO_2 into a hydrofracture zone, based on P- and S-wave data. A high-frequency piezo-electric P-wave source and an orbital-vibrator S-wave source were used to generate waves that were recorded by hydrophones as well as three-component geophones. The injection well was located about 12 m from the source well.

During the pre-injection phase water was injected into the hydrofrac-zone. The set of seismic experiments was repeated after a time interval of 7 months during which CO_2 was injected into the hydrofractured zone. The questions to be answered ranged from the detectability of the geologic structure in the diatomic reservoir to the detectability of CO_2 within the hydrofracture. Furthermore it was intended to determine which experiment (cross well or single well) is best suited to resolve these features.

During the pre-injection experiment, the P-wave velocities exhibited relatively low values between 1700-1900 m/s, which decreased to 1600-1800 m/s during the post-injection phase (-5%). The analysis of the pre-injection S-wave data revealed slow S-wave velocities between 600-800 m/s, while the post-injection data revealed velocities between 500-700 m/s (-6%). These velocity estimates produced high Poisson ratios between 0.36 and 0.46 for this highly porous ($\sim$ 50%) material. Differencing

post- and pre-injection data revealed an increase in Poisson ratio of up to 5%. Both, velocity and Poisson estimates indicate the dissolution of CO_2 in the liquid phase of the reservoir accompanied by a pore-pressure increase.

The single well data supported the findings of the cross well experiments. P- and S-wave velocities as well as Poisson ratios were comparable to the estimates of the cross well data.

The cross well experiment did not detect the presence of the hydrofracture but appeared to be sensitive to overall changes in the reservoir and possibly the presence of a fault. In contrast, the single well reflection data revealed an arrival that could indicate the presence of the hydrofracture between the source and receiver wells, while it did not detect the presence of the fault, possible due to out of plane reflections.

Key words: cross well seismic tomography, P-wave and S-wave velocities, Poisson ratio, single well seismic imaging, CO_2 sequestration, enhanced oil recovery

INTRODUCTION

A subsurface CO_2 injection pilot program is currently being operated by Chevron USA Production Company in the Lost Hills, California, oil field (Figure 1). This pilot program, which is partially funded by the U.S. Department of Energy (DOE) as an enhanced oil recovery (EOR) project, is ideally suited for design and testing of geologic sequestration concepts including subsurface monitoring techniques.

Lost Hills Diatomite

The reservoir at Lost Hills is comprised of diatomite which consists of approximately equal parts biogenic silica, clay, and silty-sands. As the diatomite is buried at higher pressures and temperatures, the silica, which is initially in a form called opal-A, undergoes a phase transition to opal-CT and subsequently to quartz (Isaacs, 1982). Hydrocarbons are found in all three phases with enhanced production from

fracturing in transition zones. Depositional laminations in the diatomite with varying silica content affect the system permeability (Graham and Williams, 1985). The layers with phase transitions may exhibit enhanced natural fracturing and therefore higher effective permeability, while other layers with lower permeability act as flow barriers.

The success of CO_2 sequestration will depend greatly on the reservoir properties. The diatomite reservoirs of central California have unusually high porosity (45-70%) and low permeability ($<$ 1 millidarcy). The pore size is $<$ 5 microns while the pore space is occupied by a mixture of water (50%), oil (45%), and gas (5%) (Perri et al., 2000). Because of the low permeability, the diatomite reservoir is developed with 5,060 m^2 (1.25 acre) well spacing. Despite this small well spacing, only 5% of the estimated 2.6 billion barrels of oil in place has been produced since discovery in 1910. In the 1970s, the production of the Lost Hills oil fields was increased by the introduction of hydrofracturing to increase the reservoir permeability. In the 1990s, water floods were added as an EOR technique. In 2000, Chevron USA decided to start a CO_2 pilot project to study the applicability of this technique to the diatomatious reservoir. Initial test were successful resulting in the recovery of 56-65% of the original oil in place (Perri et al., 2000). Despite this success, the location and migration of the CO_2 is not known and thus it was decided to use seismic borehole methods to investigate whether the presence and the location of the CO_2 can be determined.

Previous studies in carbonate reservoirs have shown that seismic velocity changes are caused by CO_2 injection, which can be spatially mapped using cross well seismic surveys (Wang et al., 1998). The seismic velocity changes can be up to 10%, which is easily detectable and mappable with modern cross well seismic surveys. Therefore, borehole seismic surveys hold promise for mapping and long term monitoring of sequestered CO_2.

Our goal is to investigate, through field testing, the suitability of cross well and single well seismic techniques for imaging subsurface CO_2 and for monitoring geologic

sequestration on a finer scale than can be achieved with seismic surface methods. In particular, it was intended to determine whether time-lapse effects can be detected by either method, and which method is best suited to detect geologic features like an interpreted fault and the gas-filled hydrofracture. In a concurrent study, other investigators are combining electromagnetic and seismic methods and use a rock properties model to estimate water and gas saturation changes, as well as pressure changes in the reservoir (Hoversten et al., 2002).

LOST HILLS CO_2 INJECTION SITE

The CO_2 injection project at Lost Hills is being operated by Chevron USA. The layout of the injection test is shown in Figure 2. There are four adjacent patterns (10,120 m^2 (2.5 acre) each) with one injection well centered in each pattern. The reservoir volume around injection well (11-8WR) is the target of the current seismic study. The data were acquired in observation wells OB-C1 and OB-C2, at a reservoir depth between 425 m and 640 m.

The injection well was hydraulically fractured and water flooding was conducted before it was decided to switch to CO_2 injection, to study the improvement in the rate of enhanced oil recovery (Perri et al., 2000). The CO_2 injection began in August 2000 at a relatively low flow rate of 3.5 million m^3 per day. The rate has been gradually increased to the current rate of 12.0 million m^3 per day per injection well. The injection pressure is held at 5.5-6.2 MPa, while the reservoir temperature is about 41^o C. The effect on seismic velocities and bulk density caused by the presence of CO_2 varies with pressure and temperature. In particular, the transition from liquid phase to gas phase has a dramatic effect on seismic properties as shown by Wang et al. (1998). This is a key point at the Lost Hills site where the injection pressure and temperature are such that a subsurface gas phase of CO_2 is expected. If such gas phase is present, the seismic visibility and mappability should be enhanced. Previous

cross well and single well seismic studies have shown the ability to detect a gas-bearing fracture (Majer et al., 1997).

SEISMIC DATA ACQUISITION

Pre-CO_2-Injection Survey

The first seismic borehole experiment was conducted in August 2000, before the end of the water flood. During this experiment a suite of cross well and single well data sets were acquired using the observation wells OB-C1 and OB-C2 (Figure 2). The first survey used a high-frequency (800 - 3500 Hz) piezo-electric P-wave source in OB-C1 that generated waves, which were recorded by 3-component wall-locking accelerometer sensors in OB-C2. The second survey used an intermediate-frequency (70 - 350 Hz) orbital-vibrator source, generating S-waves, which were recorded by the same receivers in OB-C2. The third survey was a single well imaging experiment (i.e., source and receivers in the same well) in OB-C1 using the piezo-electric source and hydrophone sensors.

During the cross well surveys, the sources and receivers covered a depth range from 400 m to 640 m. The source and receiver spacing was 1.5 m (5 ft). The piezo-electric source generated P-waves with a center frequency of about 2000 Hz, which translates into wavelengths of about 1 m, while the orbital-vibrator source generates lower frequencies between 70 Hz and 350 Hz. However, because the S-wave velocities in the reservoir are relatively low (average of 650 m/s) and the maximum S-wave energy was observed at 250 Hz, the wavelength of the shear waves is about 2.6 m. Therefore, the spatial resolution of the two data sets is comparable, based on frequency considerations alone. We will address in the next paragraph, however, that the resolution of the S-wave data during the travel time inversion, is less than that of the P-wave data.

Figure 3 shows a common receiver gather for the piezo-electric source (Figure 3a and the orbital-vibrator source (Figure 3b. The P-wave in Figure 3a shows a strong first arrival, although the waveforms appear to resonate after the onset of the wave. However, because of the good signal-to-noise ratio, it was possible to determine the first arrival times with good accuracy. The S-waves in Figure 3b were more difficult to analyze. The data indicates that for zero-offset traces and traces at low incidence angles, S-wave energy represents the first arrivals followed by tube-waves generated by wave conversion at the receiver well. For higher incidence angles, a wave, indicated as Mach-wave, is visible as first arrival passing the S-wave energy. The generation of the Mach-wave is caused by the low S-wave velocities in the medium. The Mach-waves are excited by tube-wave energy traveling up and down the source well radiating S-wave energy into the medium. These waves arrive at the receiver well with an apparent velocity faster than that of the S-waves in the medium velocity (Meredith et al., 1993). Therefore, the S-wave arrival times were only determined at low incidence angles, which limited the spatial resolution of the velocity estimates in the S-wave travel-time inversion.

The single well data, generated by the piezo-electric source, are shown in Figure 4. The data were recorded with a 15-level hydrophone string with 3 m (10 ft) spacing. The data in Figure 4 represents a common offset gather, where the offset between source and single receiver is kept constant throughout the reservoir interval. For the case of a constant-velocity medium, the moveout would be horizontal throughout the displayed depth interval in Figure 4. Similarly, variations in the arrival times of the waves indicate variations in the velocity of the medium. Three groups of waves can be recognized in the data gather. These are the direct propagating P-waves arriving at about 19 ms, followed by tube-wave energy at about 26 ms. The phases arriving prior to the P-waves represent tube-wave energy that was excited by previous shots and is reverberating in the borehole. The large tube-wave amplitudes masked any energy present in the data that may have been reflected off the hydrofracture.

Technical problems prevented the acquisition of S-wave data in the pre-injection experiment.

Post-CO_2-Injection Survey

The second seismic borehole experiment was conducted in May 2001, after a period of eight months of CO_2 injection. During this experiment a second suite of cross well and single well data sets were acquired using the same source combination as in the pre-injection experiment. However, technical changes in the interim lead to the use of hydrophones as receivers throughout the post-injection survey.

The post-injection cross well data are shown in Figure 5. The P-wave data generated with the piezo-electric source are presented in Figure 5a. It can be seen that the signal-to-noise ratio is comparable to the pre-injection data, and that the resonating character of the data is less pronounced. We attribute this observation to the use of a new hydrophone string in the receiver well. The S-wave data generated with the orbital-vibrator source are shown in Figure 5b. Similar to the pre-injection experiment, both S-wave and Mach-waves can be seen in the common receiver gather.

For the single well experiment, a recently developed tool was introduced to attenuate the effect of the large tube-wave energy in the data. This tube-wave suppressor, designed by the Idaho National Engineering and Environmental Laboratory (INEEL), is shown in Figure 6. The figure depicts the single well seismic imaging equipment that is operated in a borehole to image the surrounding medium. A piezo-electric source is connected to a 3200 m fiber-optic wireline cable, with a 24-channel analog-to-digital converter attached below. The digitizer converts the analog input signal from the hydrophones to a digital output and sends it through the fiber-optic cable to a data recorder at the surface. The tube-wave suppressor is placed between the source and the hydrophones to attenuated energy propagating from the source along the borehole to the receivers below. The tube-wave suppressor contains a rubber

bladder that is inflated with gas and kept slightly below ambient pressure of the fluid column in the well. The tube-waves, propagating past the suppressor, excite oscillations of the bladder and loose their energy during this process (Daley et al., 2002). This results in strongly attenuated tube-waves relative to the body-waves propagating through the medium outside the borehole. Figure 7 shows a common offset gather for the single well experiment using the tube-wave suppressor. The improvement over the data in Figure 4 (single well data without tube-wave suppressor) is apparent. The direct propagating P-wave is visible throughout the depth range of the reservoir, while velocity variations can be seen. There is no reverberating tube-wave energy apparent prior to the P-wave and only little energy past their original onset at 26 ms (compare to Figure 7). Because of the attenuation of the tube-waves an additional arrival becomes apparent behind the direct P-wave at about 21 ms. This energy appears to be a reflection, possibly from the hydrofracture, as we will show in a later section. Contrary to the pre-injection survey, an S-wave data set was acquired during the post-injection single well experiment. The data are presented in Figure 8. The results are similar to those in Figure 7 in that the suppression of the tube-wave energy enabled the identification of the S-waves. The shear wave arrival is visible between 37 ms and 50 ms revealing an increase in S-wave velocity with depth. Remnant tube-wave energy is visible between 25 ms and 35 ms which would have overshadowed the weaker shear wave arrival. The P- and S-waves velocities from the single well experiment will be analyzed in a later section.

CROSS WELL RESULTS

P-wave Data

In order to determine velocity estimates of the reservoir, the first arrival times for P- and S-waves were determined from the data. The travel time data was inverted

using a straight ray back-projection algorithm (Peterson et al., 1985). The inversion process included static time-shifts for each source and receiver location, to account for possible local anomalies around the borehole in the vicinity of sources and receivers which could map into the velocity estimates if not corrected for.

The P-wave velocity estimates are shown in Figure 9. The results are presented within the reservoir interval from 420 m and 640 m. The location of the sources and receivers are denoted by stars and inverted triangles within the boreholes OBC1 and OBC2, respectively. The geologic layering is indicated by the black lines, while the red line represents the location of an interpreted fault. Figure 9a represents the velocity estimates for the pre-injection experiment. It can be seen that the velocity varies smoothly throughout the reservoir and increases with depth, representing a gradual phase transformation of the diatomite. The increase in pressure and temperature with depth causes an irreversible phase transformation, during which the structure of the diatoms is destroyed by compaction causing a transformation from opal-A to opal-CT silica (Bilodeau, 1995). The effect is a significant reduction in porosity and an increase in velocity as seen in Figure 9a. An apparent transition from slower to higher velocities (1750-1850 m/s) can be seen at about 530 m depth which is manifested by a change in lithology and trace fossil record (Perri et al., 2000). Figure 9b shows the velocity estimates of the post-injection experiment. It can be seen that the overall velocity dropped about 50-80 m/s throughout the reservoir. The main velocity structure is similar to that of the pre-injection test with no apparent localized change in the pattern that could indicating the location of CO_2. To better analyze the subtle temporal changes between the pre- and post-injection data, we compute the differences pre-minus-post between the two velocity tomograms. The results are displayed in Figure 9c. The black dashes indicate the location of the injection intervals in the reservoir. It can be seen that the maximum velocity decreases are $\sim$ 90 m/s ($\sim$ 5%), and occurred above the injection interval between 440-480 m depth, at intermediate depth from 540-560 m, and in the lower part of the reservoir

at 600 m depth. The top anomaly appears to be located between well OB-C2 and the fault, which seems to be partly inhibiting the extension of the anomaly towards well OB-C1. If this is a manifestation of the presence of CO_2, the gas must have migrated upwards above the fractured interval, possibly by an extension of the fracture to shallower depth.

S-wave Data

The pre-injection S-wave velocity estimates (Figure 10a) corroborate the results of the P-wave data from above. The transition from upper to lower reservoir diatomite is clearly visible at about 530 m depth. Although the inversion resulted in very low S-wave velocity estimates between 550-850 m/s, these values are not uncommon for this soft reservoir rock (Bourbié et al., 1987, Morea, 2002, personal correspondance). The S-wave velocity structure is similar to that of the P-waves with a low velocity layer between 440-480 m, followed by intermediate velocities between 500-520 m depth, and a sharp transition to lower reservoir properties at 530 m depth. However, the spatial resolution of the S-wave data is limited by the predominantly sub-horizontal ray coverage. The post-injection results in Figure 10b reveal a velocity drop of about 50-80 m/s while the overall structure of the velocity image remains the same. Again, no apparent location of CO_2 is visible. The differenced results in Figure 10c reveal a maximum decrease of 75 m/s ($\sim$ 9%) (the anomaly along the top of the image of -120 m/s is less reliable because of the limited ray coverage along the top of the reservoir, which was different for the pre- and post S-wave survey). In comparison to the maximum P-wave velocity difference at 440-480 m between well OB-C2 and the fault, the S-wave velocities reveal an intermediate decrease of 60 m/s for the same location. However, in the central and bottom part of the reservoir (560-580 m and 600 m depth) equally strong velocity decreases are visible.

The time lapse velocity estimates for P- and S-waves show good correlation

throughout the reservoir, although they represent independent data sets as they were excited by different seismic sources. At this point, however, the common interpretation does not yield a unique answer about the state of CO_2 in the reservoir. If CO_2 is present in gas form and the pore pressure does not change (i.e, gas displaces pore fluid), the P-wave velocity would decrease while the S-wave velocity would remain constant, as the S-wave is not sensitive to changes in gas or fluid saturation. However, since the S-wave velocities decrease, a pressure increase is likely to have occurred during the CO_2 injection phase. In this case, both P- and S-wave velocities would decrease since the differential pressure (confining-minus-pore pressure) would decrease. This scenario is possible for the case of free gas as well as for the case of the dissolution of CO_2 into the liquid phase in the reservoir. To answer the question of the state of the CO_2 in the reservoir, we calculate the Poisson ratio and interpret the results in the next section.

Poisson Ratio

The Poisson ratio (PR) is calculated based on the velocity estimates for P- and S-waves shown in Figures 9 and 10 as

$$\nu = \frac{0.5\,(V_p/V_s)^2 - 1}{(V_p/V_s)^2 - 1}. \tag{1}$$

Figure 11a shows the PR for the pre-injection experiment. The estimates mimic the trend of the P- and S-wave velocity estimates, which is not necessarily expected, because the velocity effects could cancel in Equation 1. The PR shows a clear separation into the upper and lower reservoir diatomite with the transition at 530 m depth, as shown before. The high PR in the upper reservoir section is caused by the low S-wave velocity estimates, however, PR of 0.42-0.45 are not uncommon for this highly porous rock (Bourbié et al., 1987). The decrease in PR with depth is a sign for the compaction of the diatomes accompanied by a decrease in density (Bilodeau, 1995).

The post-injection estimates (Figure 11b) are similar to the pre-injection values, with the exception of higher values in the upper reservoir (440-460 m), where the S-waves velocities were particularly low.

The difference in PR is shown in Figure 11c. It can be seen that the time-lapse changes resulted in an increase in PR throughout the reservoir (the negative values a the bottom are an artifact of the inversion process caused by limited ray coverage). These results support the preliminary findings derived from the velocity inversions. If a free gas was present and the pore-pressure increases (which is necessary in our case to explain the drop in S-wave velocity) the PR would decrease as shown by Dvorkin et al. (1999) and Mallick (2001). However, if the gas is in solution (i.e., the medium is fluid saturated) and the pore- pressure increases, the PR increases as reported by Detournay and Cheng (1993), Dvorkin et al. (1999), and Simpson (1985). In a similar study Dvorkin and Nur (1996) showed that for water saturated high porosity sandstone (20-40%) the PR increases with decreasing confining pressure. To evaluate the estimates for the PR as shown in Figure 11c, we calculate the change in PR using a rock properties model based on Gassmann's equation (Gassmann, 1951). The result is an increase in PR with an average value of 0.0045. In comparison, the average value of the increase in PR in Figure 11c is 0.0074 ± 0.0052 yielding estimates in line with the prediction of the rock properties model (Hoversten et al., 2002).

Thus a possible conclusion that can be drawn from the PR results is that CO_2 dissolves into the liquid phase in the reservoir rock and increased the pore pressure in several compartments inside the reservoir. Figure 11c suggest that CO_2 migrated horizontally in the lower section of the reservoir around 570 and 600 m depth. The strong increase at the top of the reservoir above 440 m is likely an artifact resulting from low resolution of the S-wave estimates. However, the slight increase visible above the top of the injection interval may indicate an over-pressurization of the reservoir caused by an upward migration of the CO_2, as the PR should have remained constant otherwise. However, it is also possible that some of the regions that reveal an increase

in PR have undergone a pore-pressure increase caused by the injection process without the CO_2 actually reaching these zones.

In the following, the results of the cross well experiment will be compared to the single well data.

SINGLE WELL RESULTS

Direct Waves

A conceptual model of a single well seismic experiment is shown in Figure 12. A source emits seismic energy which propagates to receivers below (a reverse geometry where the source is located below the receivers has also been used for single well imaging in the past). The direct waves reach farther into the medium compared to sonic logging because the source-receiver offset and the wavelengths of the waves are longer. At the same time, waves propagate outwards from the well and reflect off interfaces above and below and off features like faults and fractures that may be present in the medium.

The direct arrival times of the P-waves (pre- and post-injection) and the S-waves (post-injection) were determined from the single well data collected in well OB-C1. The results are plotted in Figure 13. The pre-injection results are shown in Figure 13a. The thick gray line represents the velocity measurements from the single well data, while the thin black line is an average velocity combining the estimates of the three pixels adjacent to the source well OBC1 (horizontal average over 5m). Although static source corrections have been accounted for, the average yields a better comparison because the P-waves of the single well data propagate farther out from the well. The different depth ranges are the result of different acquisition intervals caused by different receiver strings and source-receiver offsets. The fit is good, nevertheless, indicating that the near borehole effects (i.e., borehole cement, borehole

anulus) present in many sonic log velocity data, play only a minor role in the present case as the longer wavelengths integrate the effects farther away from the borehole. This result corroborates the velocity estimates of the travel time inversion. The post-injection P-wave results are presented in Figure 13b. The dashed line represents results of ultrasonic velocity measurements by Chevron, USA, on cores taken 126 m west of the CO_2 injection site (Morea, 2002, personal correspondance). The overall fit between the single- and cross well results is good, although the single well data did not cover the lowermost section of the reservoir. Although the P-wave velocity measurements reveal more variation throughout the depth range, the overall values fall within the range of the field measurements. The comparison of the S-wave field data in Figure 13c reveals a good fit even down to details in the velocity structure (i.e., velocity increase with depth, velocity inversion between 460-480 m depth). The ultrasonic results show higher values in the upper reservoir, while they match the field data in the lower reservoir section. Finally, the post-injection PR is plotted in Figure 13d. The result of the single well experiment is limited to the depth range where post P- and S-wave data overlap. However, even for this limited depth range the fit between the two graphs representing the field data is very good, revealing an overall decrease of the PR with increasing reservoir depth. The lower values at the bottom of the reservoir are in accordance with the transition to more clay bearing diatomite, which exhibit PR between 0.35-0.40. The PR of the core data was computed based on equation (1) using the ultrasonic velocities as shown in Figure 13a and 13b. As expected from the trend of the S-wave data, the fit is better in the lower half of the reservoir.

The fact that the ultrasonic velocities and hence the PR are comparable to the field data is remarkable by itself, as it is generally believed that laboratory data yield higher velocity estimates. The cores did not reveal major fractures, which are expected to be present in the CO_2 injection area. A possible explanation is that the seismic velocities are governed by the pore structure and the high porosity ($\sim$

50%) of the diatomite. Although the difference in wavelengths between the field data ($\sim$ m) and the ultrasonic lab data ($\sim$ mm) is considerable, both are still much larger than the pore size ($\sim \mu$m), such that the sampled medium exhibits the same degree of heterogeneity based on its pore structure. Although the introduction of hydrofractures at the field scale adds a degree of structural heterogeneity to the medium, which increases the permeability of the reservoir, it may not necessarily increase the already high porosity value. Therefore, in the case of diatomite, the seismic waves may not be as much affected by the presence of hydrofractures as by the high porosity value. However, the time lapse experiments shown in this study indicate the effectiveness of this method to monitor temporal changes in the reservoir.

In summary, the results of the single well data independently confirm the results of the cross well experiment. Therefore, when available, both experiments should be run simultaneously to determine the reliability of the velocity estimates.

Reflected Waves

In addition to the direct wave, the single well data revealed an additional phase that was pointed out in Figure 7 arriving between 21 and 24 ms. It was investigated whether this event could be a reflection off the hydrofracture between the observation wells OBC1 and OBC2. Because the moveout of the reflection is horizontal, it is unlikely that it represents a reflection of the fault as it cuts through the cross section in Figures 9 -11 at an angle. It is more likely that this event reflects off a vertical feature adjacent to the well throughout the reservoir. To process this event, common mid point (CMP) gathers were created with a spacing of 0.3 m (1 ft) while the direct wave was muted out up to 2-3 ms past its first arrival time. Three neighboring CMP gathers were binned to create a maximum fold of 24. Different stacking velocities were used to investigate the coherency of the reflections. It was found that a stacking velocity of 1675 m/s resulted in maximum coherency in the reflected data. The

details of this procedure are presented in Daley et al. (2002). The final step involved a Kirchoff depth migration using a variable velocity field as estimated by the travel time inversion in Figure 9b. The result of the migration is presented in Figure 14. The traces represent 1 m (3 ft) bins. A strong reflection event is visible at a radial distance of 10-12 m from the well at a depth interval between 450-550 m. A second event is visible between 370-410 m depth at the same distance from the well. To interpret these arrivals, the geometry of the injection wells is shown in Figure 15. The two observation wells are deviated showing a separate top and bottom location. However, the deviations occur between 122 and 244 m and don't affect the measurements in the reservoir section (420-640 m) where the wells are reasonably straight, as can be seen by the source and receiver locations in Figures 9, 10, and 11. The bottom locations of the injection well are indicated by the circles at a distance of about 12 m and 15 m from OB-C1. The original water injection well is labeled 11-8W while a parallel CO_2 injection interval (11-8WR), originating from the water injector, was drilled in the lower parts of the reservoir (see black dashed line in Figures 9, 10, and 11). The strike of the two hydrofractures, indicated by the parallel lines, was derived from surface tiltmeter measurements (Perri et al., 2000). The scale indicates that the event in Figure 12 correlates in space with the location of the hydrofracture and not the CO_2 fracture. However, discussions with engineers at Chevron, USA, revealed that upon CO_2 injection the fracture 11-8W showed an increase in pressure first, suggesting that a flow path exist for the CO_2 between the new and the old fracture. This is not unlikely, because the water-flood in 11-8W has been ongoing since 1991, which has undoubtly affected the immediate area of the hydrofracture. Similar observations of conductivity and break throughs between neighboring fractures have been observed in wells adjacent to the CO_2 pilot (Perri et al., 2000). Thus it is possible that the event in Figure 14 indicates the presence of the original hydrofracture 11-8W. The extension of this event to depths shallower than the injection interval indicates that the fracture migrated upwards in the reservoir, an occurrence that was not originally

planned. A closer look at Figure 14 may indicate a secondary arrival around 16 m radial distance from observation well OB-C1 that correlates with the location of the CO_2 injection fracture in Figure 15. In this case, the difference in reverberations between the two reflection events may indicate that the younger fracture has less aperture than the older one (i.e., a single fracture versus a fractured zone), which can be expected considering the history of the water injection in the past. However, the data quality is not good enough to draw a final conclusion for this hypothesis.

CONCLUSIONS

The goal of the current experiment was to investigate whether the location and migration of CO_2 in geologic sequestration processes can be imaged with seismic borehole methods. The time-lapse borehole experiment was conducted over a period of one year, during which a series of cross- and single well experiments resulted in the successful acquisition of P- and S-wave data. The addition of a tube-wave suppressor during the post-injection phase resulted in a reduction of tube-wave amplitudes, such that shear wave and reflected waves were visible in the data records. However, the comparison of seismic amplitudes was not possible, because different receiver types were used during the pre- and post-injection phase.

The separate results of the cross well experiments showed no clear indication of the location of the fault between the two observation holes. However, differencing the P-wave velocity estimates revealed the possible location in form of an abrupt termination of a velocity anomaly. At the same time there was no evidence of the hydrofracture in the cross well results.

The P-wave and S-wave velocity estimates showed a decrease in value over the course of the CO_2 injection phase, indicating a possible increase in pore pressure throughout the reservoir. However, using the velocity estimates only, it was not possible to determine whether the CO_2 exists in gas from or whether it dissolved

into the liquid phase in the reservoir. After the Poisson ratio was calcultated from the velocities, however, it was concluded that the CO_2 had dissolved into the liquid phase, as the time-lapse results revealed an increase in PR. This shows the advantage of simultaneous acquisition of P- and S-wave data. The tomographic images suggested the extension of the hydrofracture to a shallower section of the reservoir above the intended fracture interval.

The concurrent acquisition of single well data enabled us to verify the results of the cross well survey. The wavelengths excited in the single well experiment are long enough to sample the medium in the vicinity of the well without too much interference from borehole effects as in the case of sonic logging. Therefore, the velocity estimates are more representative of the medium, and, as in our case, could be used to independently verified the results of the cross well survey. Furthermore, the single well data indicated the presence of a reflection event that coincided with the location of the hydrofracture between the observation wells. At the same time, no indications of the presence of the fault were observable in the singe well data.

The combination of seismic cross- and single well experiments appears to be suitable to investigate the presence of CO_2 in subsurface reservoirs. The advantage of seismic borehole over surface methods is a better resolution, which allows to detect the subtle changes in velocity and the spatial distribution of CO_2 in the subsurface. Cross well tomography offers the advantage of imaging a larger area for integral time-lapse changes, while single well imaging appears to be suited for direct target detection as in the case of a vertical hydrofracture. Both experiments can be readily conducted at the same time and offer the possibility to verify common results, while they provide complementary information that adds to the general understanding of the reservoir properties.

ACKNOWLEDGEMENTS

The authors like to acknowledge reviews by Valeri Korneev, and Daniel Hawkes. Thanks to Mike Morea and Chevron USA Production for their generous help with field information, and the release of the ultrasonic core data. This work was supported by the GEO-SEQ project of the DOE National Energy Technology Laboratory (NETL) under contract no DE-AC03-76SF000098. Support was also provided by Chevron USA Production Co. and the National Petroleum Office under Contract No. DE-FC22-95BC14938, Class III Field Demonstration Project. Data processing was carried out at Berkeley Lab's Center for Computational Seismology, while field work and data collection were supported by Berkeley Lab's Geophysical Measurement Center. Both centers are supported by the Director, Office of Science, Office of Basic Energy Sciences, Division of Engineering and Geosciences, of the U.S. Department of Energy under Contract No. DE-AC03-76SF00098.

REFERENCES

Bilodeau, B. J., 1995, Determining Water Saturation in Diatomite using Wireline Logs, Lost Hills Field, California: Proceedings SPE/AAPG Western Regional Meeting, SPE 29653, pp. 369-382.

Bourbié, T., Coussy, O., Zinszner, B., 1987, Acoustics of Porous Media: Gulf Publishing Company, Houston, 1987, pp. 334.

Daley, T. M., and Cox, D., 2001, Orbital vibrator seismic source for simultaneous P- and S-wave cross well acquisition: Geophysics, Vol. 66, No.5, pp. 1471-1480.

Daley, T. M., Gritto, R., Majer, E. L., West, P., 2002, Tube-wave suppression in single-well seismic acquisition: Geophysics, submitted.

Detournay, E., Cheng, H., 1993, A short course on poroelasticity in rock mechanics: constitutive equations - theoretical background: Proc. U.S. Rock Mech. Symp., 34th, pp. 1-28.

Dvorkin, J., and Nur, A., 1996, Elasticity of high-porous sandstones: Theory for two North Sea data sets, Geophysics, Vol. 61, No. 5, pp. 1363-1370.

Dvorkin, J., Mavko, G., Nur, A., 1999, Overpressure detection from compressional- and shear-wave data, Geophys. Res. Lett., Vol. 26, No. 22, pp. 3417-3420.

Gassmann, F., 1951, Elasticity of porous media: Über die Elastizität poröser Medien, Vierteljahrschrift der Naturforschenden Gesellschaft, Vol. 96, pp.1-23.

Graham, S. A., and Williams, L. A., 1985, Tectonic, depositional and diagenetic history of Monterey formation (Miocene), central San Joaquin basin, California: AAPG Bulletin, March, pp. 385-411.

Hoversten, G. M., Gritto, R., Washbourne, J., Daley, T. M., 2002, CO_2 Gas/Oil Ratio Prediction in a Multi-Component Reservoir by Combined Seismic and Electromagnetic Imaging: Geophysics, *submitted.*

Isaacs, C. M., 1982, Influence of rock composition on the kinetics of silica phase changes in the Monterey Formation, Santa Barbara area, California: Geology, Vol. 10, pp. 304.

Mallick, S., 2001, AVO and elastic impedance: The Leading Edge, Vol.20, No.10, pp. 1094-1104.

Majer, E. L., Peterson, J. E., Daley, T. M., Kaelin, B., Queen, J., D'Onfro, P., and Rizer. W, 1997, Fracture detection using cross well and single well surveys: Geophysics, Vol. 62, No. 2, pp. 495-504.

Meredith, J. A., Toksoz, M. N., Cheng, C. H., 1993, Secondary shear waves from source boreholes: Geophysical Prospecting, Vol. 41, No.3, pp. 287-312.

Perri, P. A., Emanuele, M. A., Fong, W. S., and Morea, M. F., 2000, Lost Hills CO_2 pilot: evaluation, design, injectivity test results and implementation: Proceedings SPE/AAPG Western Regional Meeting, SPE 62526, pp. 13.

Peterson, J. E., Paulson, B. N., and McEvilly T. V., 1985, Applications of algebraic reconstruction techniques to cross hole seismic data: Geophysics, **50**, No. 10, pp. 1566-1580.

Simpson, G., 2001, Influence of compression-induced fluid pressures on rock strength in the brittle crust, J. Geophys. Res., Vol. 106, No. B9, pp. 19,465-19,478.

Wang, Z., Cates, M. E., and Langan, R. T., 1998, Seismic monitoring of a CO_2 flood in a carbonate reservoir: A rock physics study: Geophysics, Vol. 63, No. 5, pp. 1604-1617.

Wilt, M., Schenkel, C., Daley, T. M, Peterson, J. E., Majer, E. L., Murer, A. S., Johnston, R. M., Klonsky, L., 1997, Mapping Steam and Water Flow in Petroleum Reservoirs:, SPE Reservoir Engineering, Vol.12, No.4, pp.284-287.

FIGURES

FIG. 1. Map indicating the location of the Lost Hills and nearby oil fields in the San Joaquin basin (from Chevron, USA).

FIG. 2. CO_2 injection site with the location of the injector (11-8WR) and the two observation wells (OB-C1 and OB-C2). The blue lines indicate the 4 injection patterns, while the green contour lines represent the top of the diatomic reservoir. The red lines are interpreted faults projected onto the top of the reservoir (from Chevron, USA).

FIG. 3. a) Common receiver gather for the pre-injection cross well experiment with the piezo-electric source (receiver elevation is 460 m). b) Common receiver gather for the pre-injection cross well experiment with the orbital-vibrator source.

FIG. 4. Common offset gather of pre-injection single well data generated with the piezo-electric source.

FIG. 5. a) Common receiver gather for the post-injection cross well experiment with the piezo-electric source (receiver elevation is 460 m). b) Common receiver gather for the post-injection cross well experiment with the orbital-vibrator source.

FIG. 6. Single well seismic data acquisition system. The sketch displays the system including the piezo-electric source, tube-wave suppressor, and hydrophones.

FIG. 7. Common offset gather of post-injection single well data generated with the piezo-electric source. The suppression of tube-wave energy produced visible reflected energy.

FIG. 8. Common offset gather of post-injection single well data generated with the orbital vibrator source. The suppression of tube-wave energy produced a strong shear-wave arrival.

FIG. 9. P-wave velocity estimates based on travel time data. a) Pre-injection estimates. b) Post-injection estimates. c) Result of differencing the Pre-Post injection estimates. The black dashes represent the CO_2 injection intervals.

FIG. 10. S-wave velocity estimates based on travel time data. a) Pre-injection estimates. b) Post-injection estimates. c) Result of differencing the Pre-Post injection estimates. The black dashes represent the CO_2 injection intervals.

FIG. 11. Poisson ratio based on the P- and S-wave velocity estimates in Figures 9 and 10. a) Pre-injection ratio. b) Post-injection ratio. c) Result of differencing the Pre-Post injection ratios. The black dashes represent the CO_2 injection intervals.

FIG. 12. Wave propagation in single well seismic data acquisition. The sketch displays the principle of wave propagation from the source to the receivers along direct or reflected ray paths.

FIG. 13. Comparison between cross well and single well estimates of the velocities and the Poisson ratio. The thin line represents a 5 m horizontal average of estimates along the source borehole from tomographic studies, while the thick line represents the results of the single well study. a) Pre-injection P-wave estimates. b) Post-injection P-wave estimates. c) Post-injection S-wave estimates. d) Post-injection Poisson ratio.

FIG. 14. Results of Kirchoff depth migration using a variable velocity field as estimated from the P-wave travel time inversion. A strong reflection is visible at a

radial distance of 10-12 m over a depth interval from 450-550 m while a weaker event is located between a depth of 370-410 m.

FIG. 15. Geometry of the observation and injection wells. The circles at 12 m and 15 m radial distance from OB-C1 represent respectively, the bottom of 11-8W (the original water injection well) and 11-8WR (the secondary CO_2 injection well which was drilled as a parallel section at the bottom of the orignal borehole 11-8W).

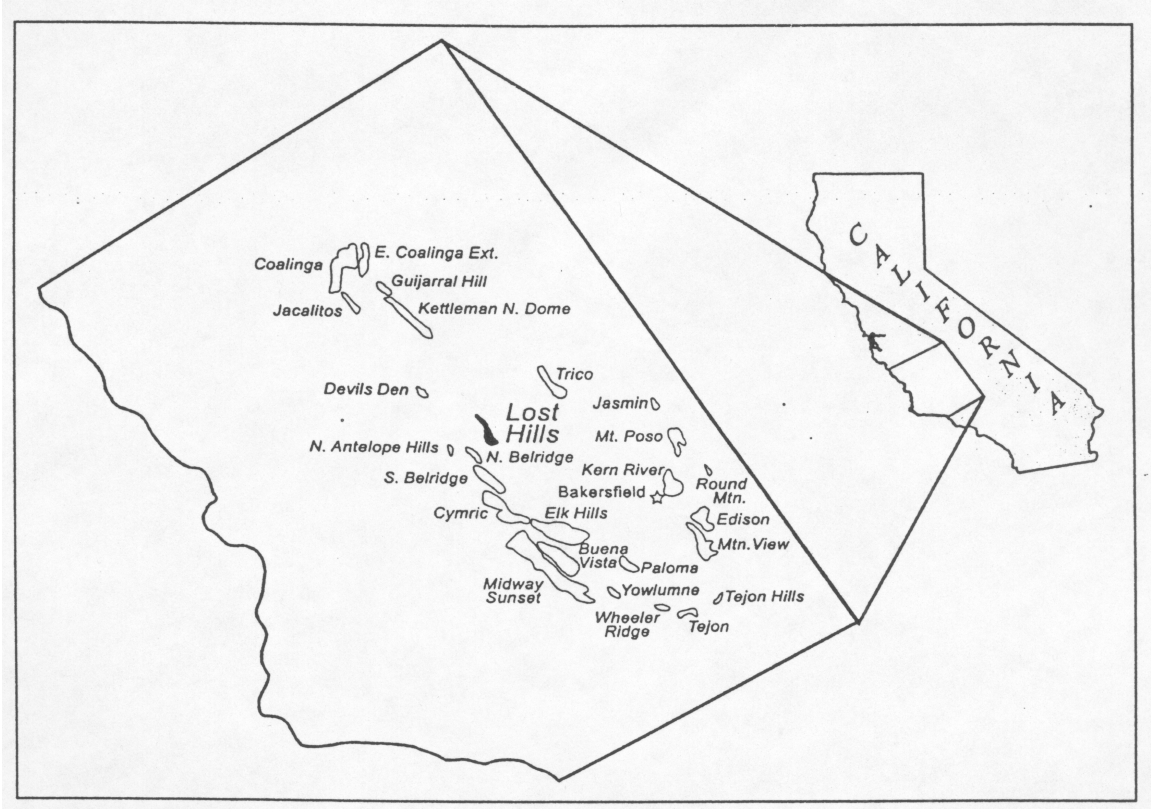

FIG. 1. Map indicating the location of the Lost Hills and nearby oil fields in the San Joaquin basin (from Chevron, USA).

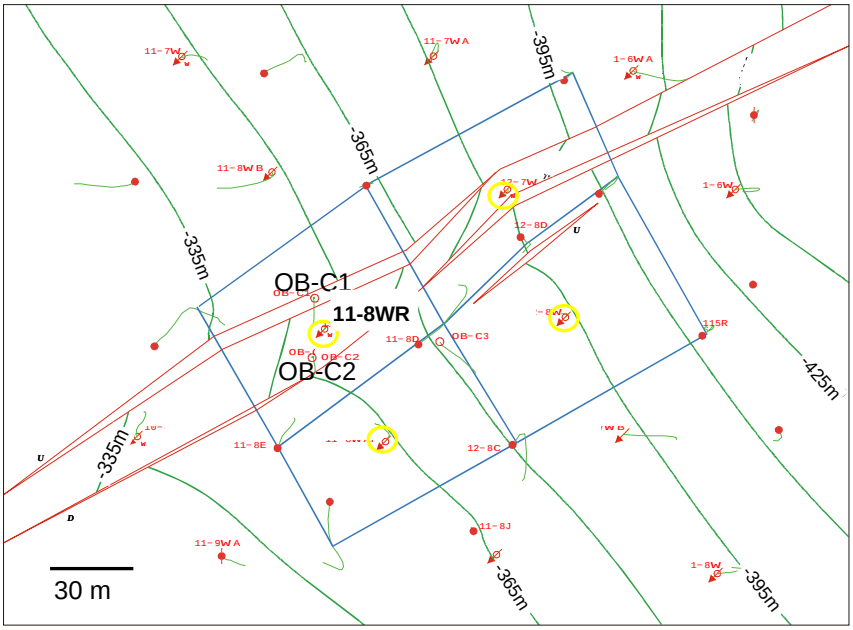

FIG. 2. CO_2 injection site with the location of the injector (11-8WR) and the two observation wells (OB-C1 and OB-C2). The blue lines indicate the 4 injection patterns, while the green contour lines represent the top of the diatomic reservoir. The red lines are interpreted faults projected onto the top of the reservoir (from Chevron, USA).

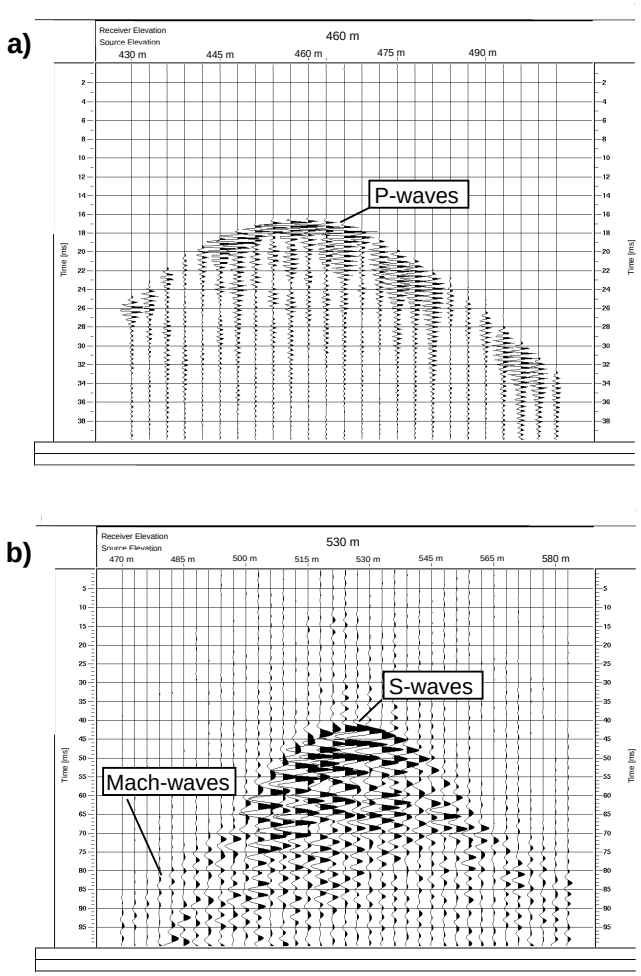

FIG. 3. a) Common receiver gather for the pre-injection cross well experiment with the piezo-electric source (receiver elevation is 460 m). b) Common receiver gather for the pre-injection cross well experiment with the orbital-vibrator source.

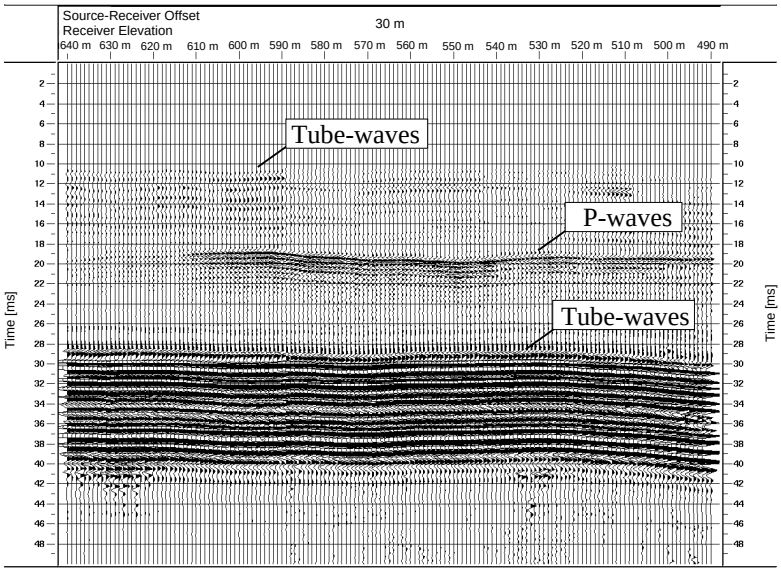

FIG. 4. Common offset gather of pre-injection single well data generated with the piezo-electric source.

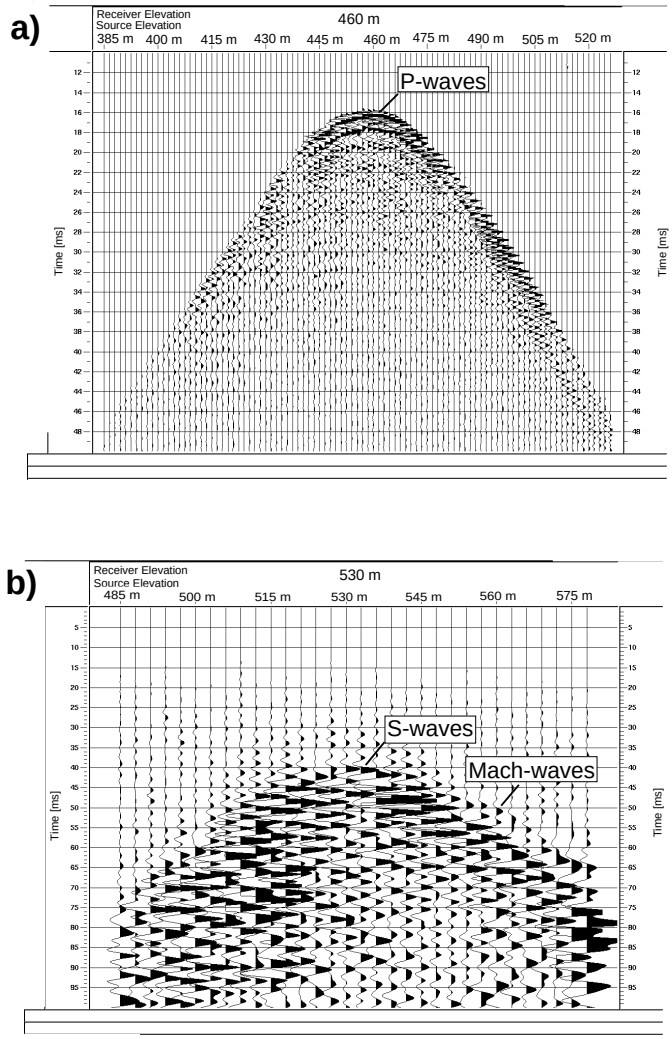

FIG. 5. a) Common receiver gather for the post-injection cross well experiment with the piezo-electric source (receiver elevation is 460 m). b) Common receiver gather for the post-injection cross well experiment with the orbital-vibrator source.

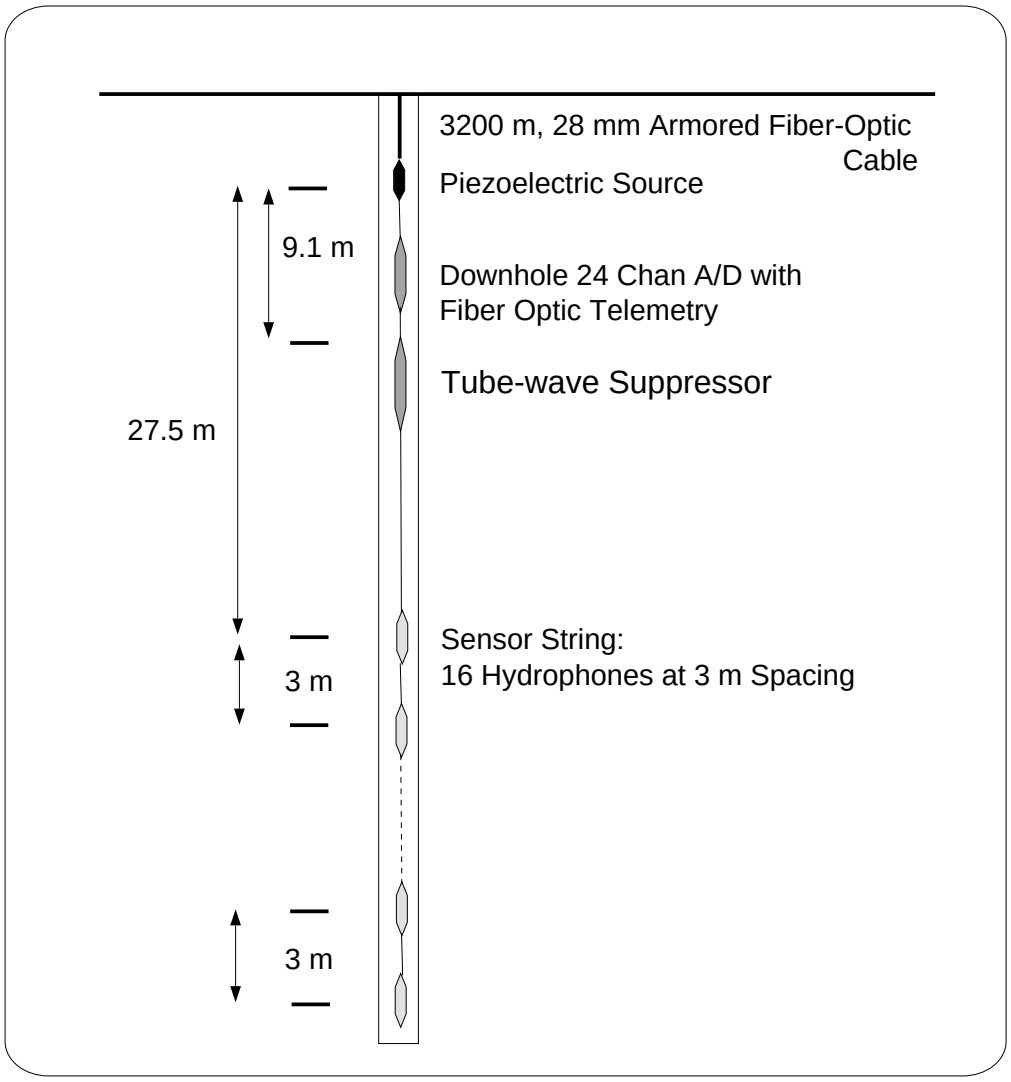

FIG. 6. Single well seismic data acquisition system. The sketch displays the system including the piezo-electric source, tube-wave suppressor, and hydrophones.

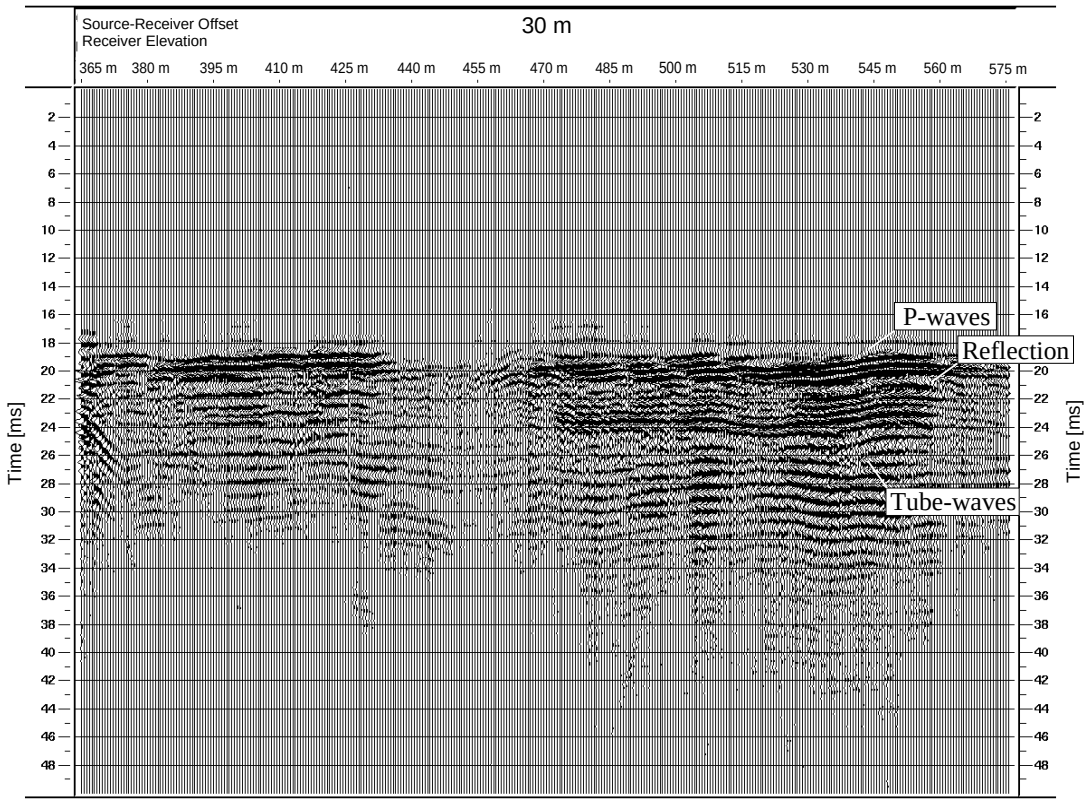

FIG. 7. Common offset gather of post-injection single well data generated with the piezo-electric source. The suppression of tube-wave energy produced visible reflected energy.

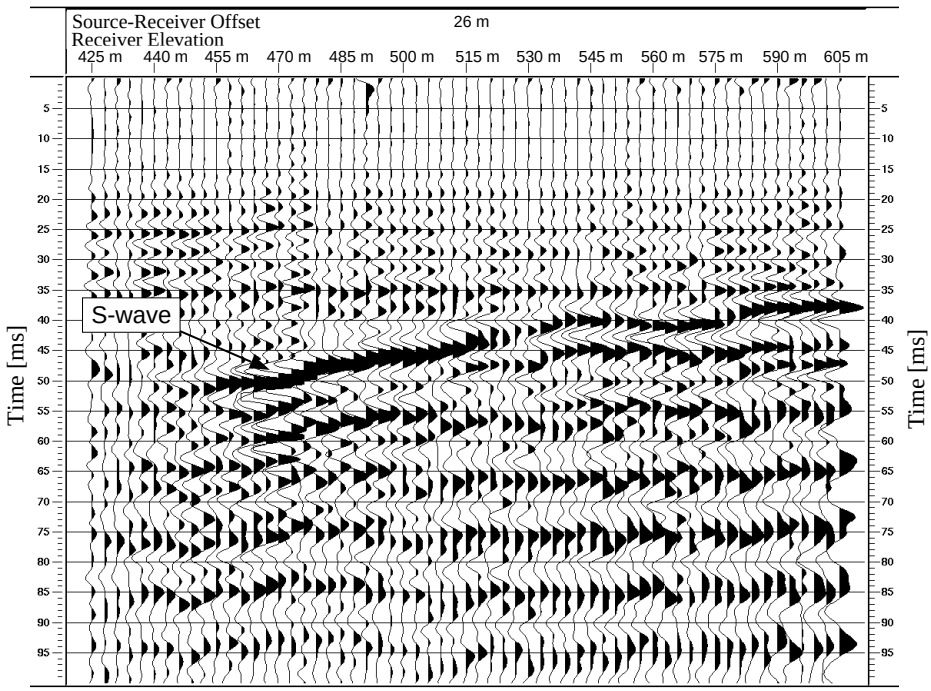

FIG. 8. Common offset gather of post-injection single well data generated with the orbital vibrator source. The suppression of tube-wave energy produced a strong shear-wave arrival.

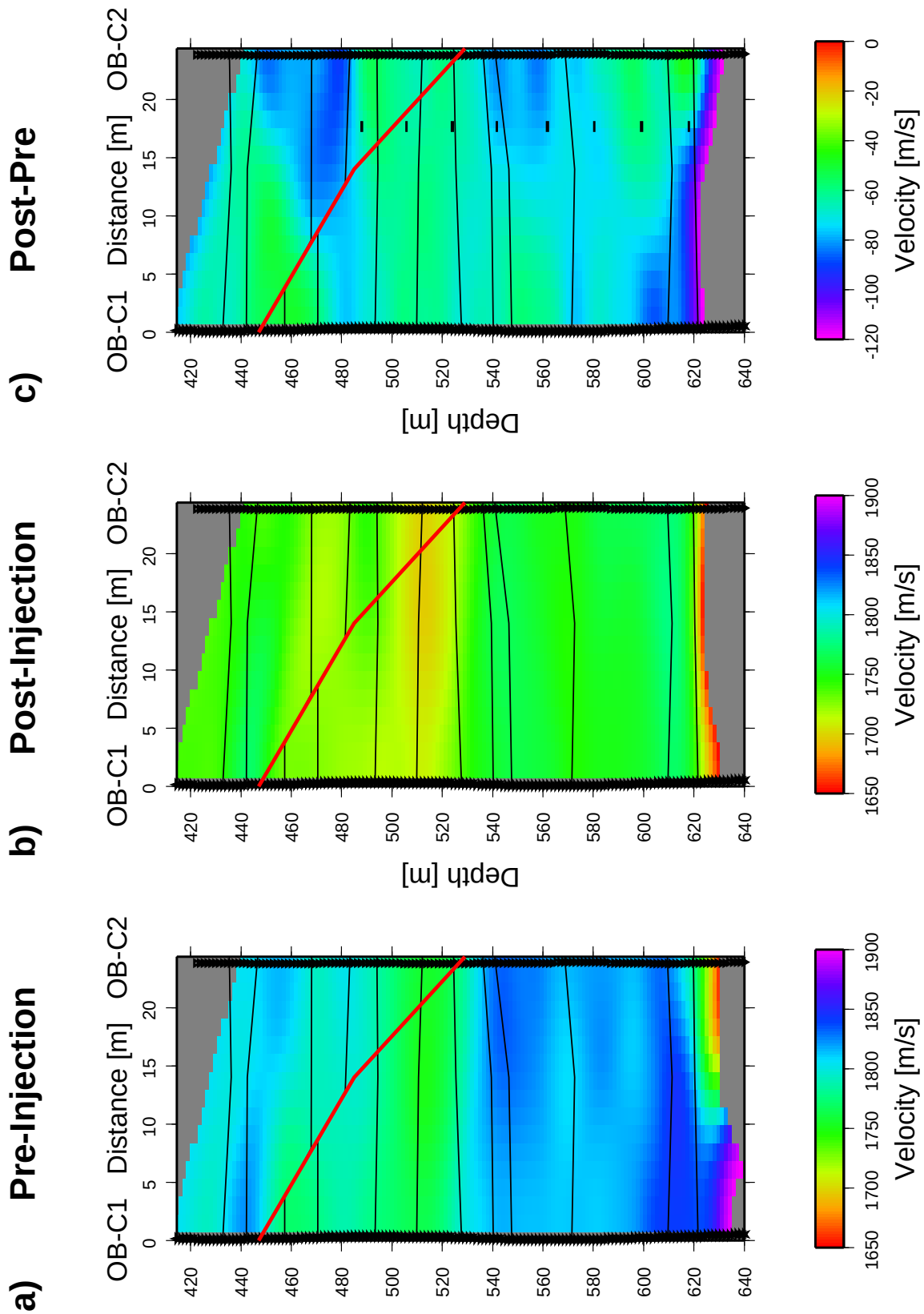

FIG. 9. P-wave velocity estimates based on travel time data. a) Pre-injection estimates. b) Post-injection estimates. c) Result of differencing the Pre-Post injection estimates. The black dashes represent the CO_2 injection intervals.

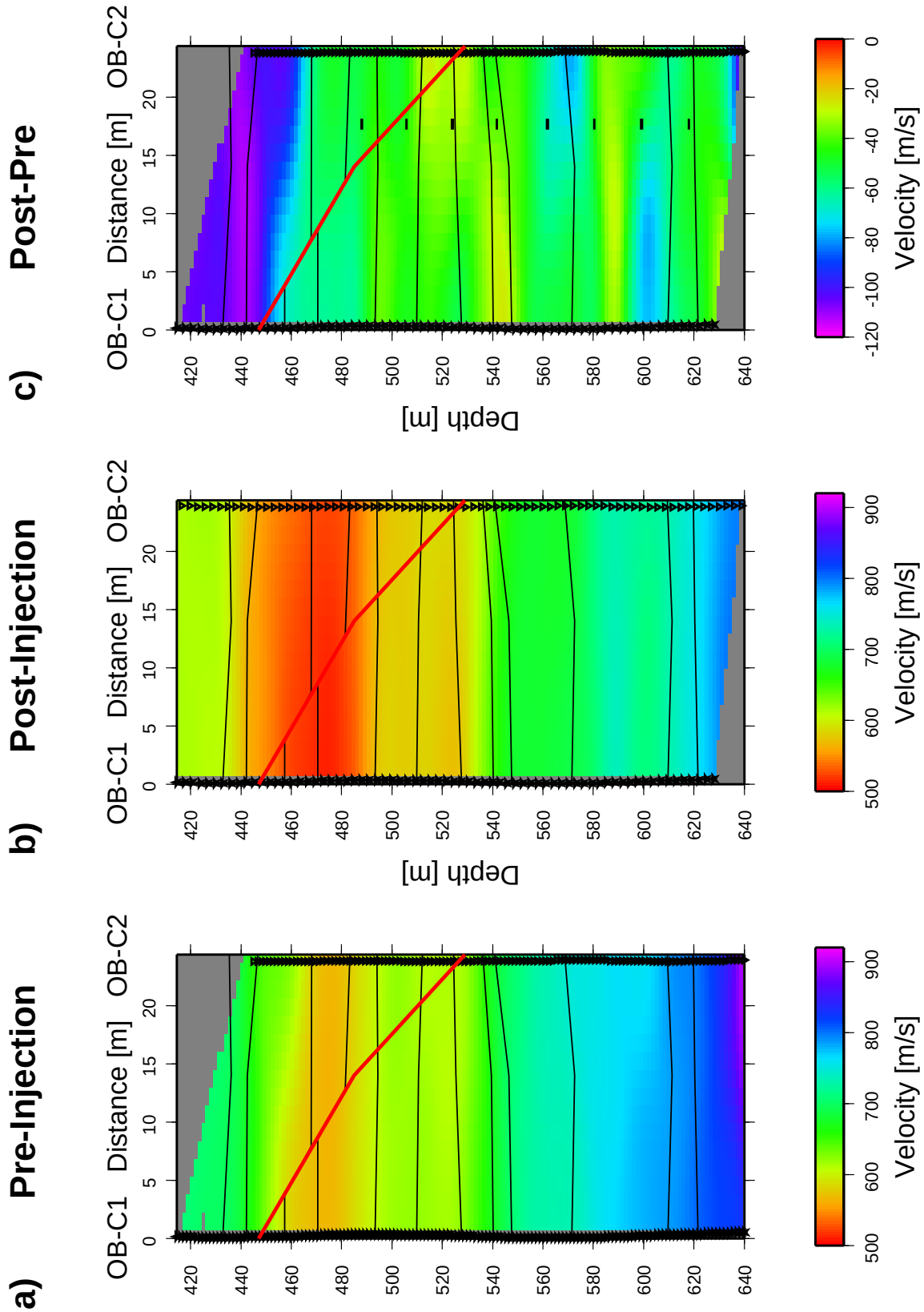

FIG. 10. S-wave velocity estimates based on travel time data. a) Pre-injection estimates. b) Post-injection estimates. c) Result of differencing the Pre-Post injection estimates. The black dashes represent the CO_2 injection intervals.

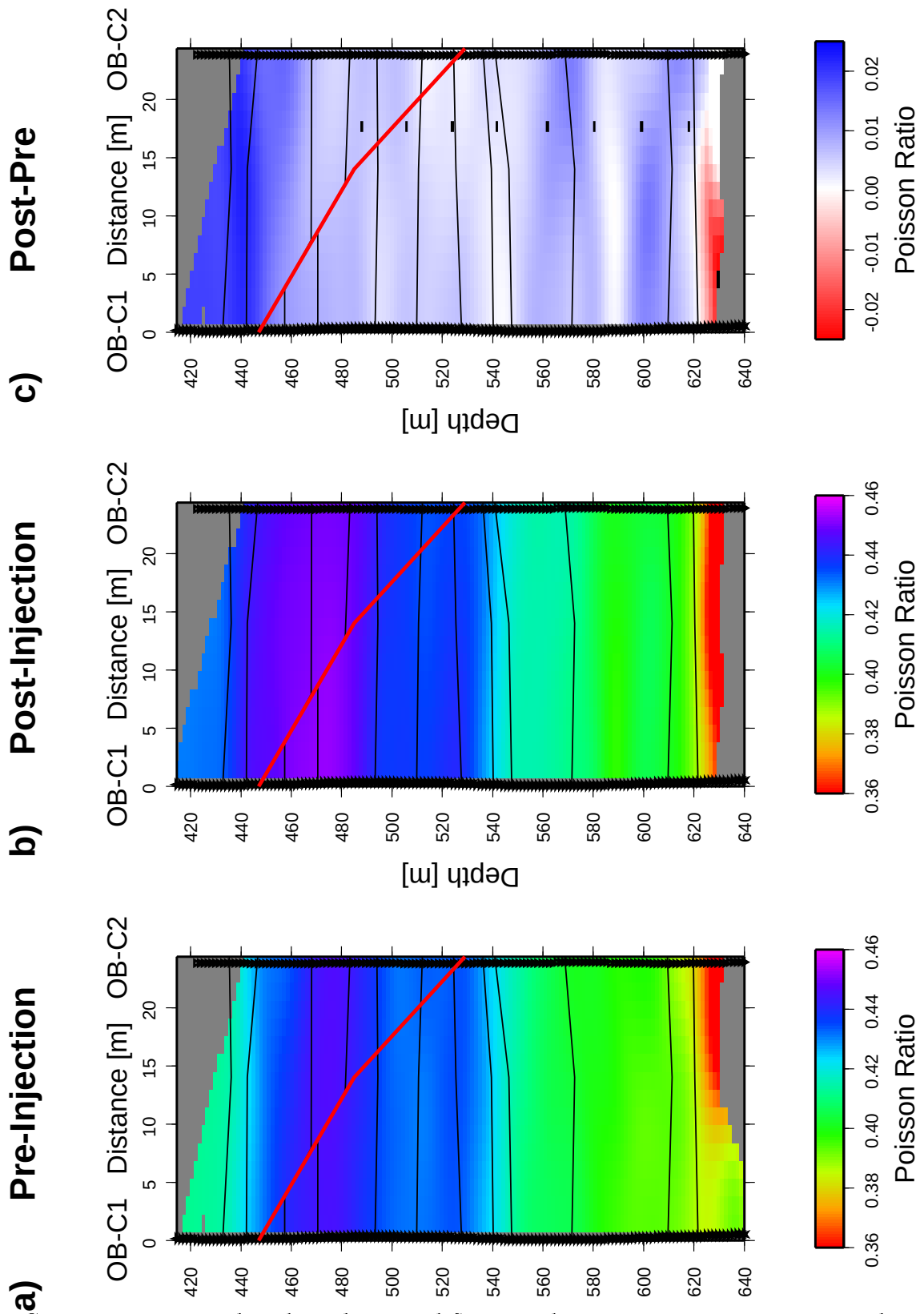

FIG. 11. Poisson ratio based on the P- and S-wave velocity estimates in Figures 9 and 10. a) Pre-injection ratio. b) Post-injection ratio. c) Result of differencing the Pre-Post injection ratios. The black dashes represent the CO_2 injection intervals.

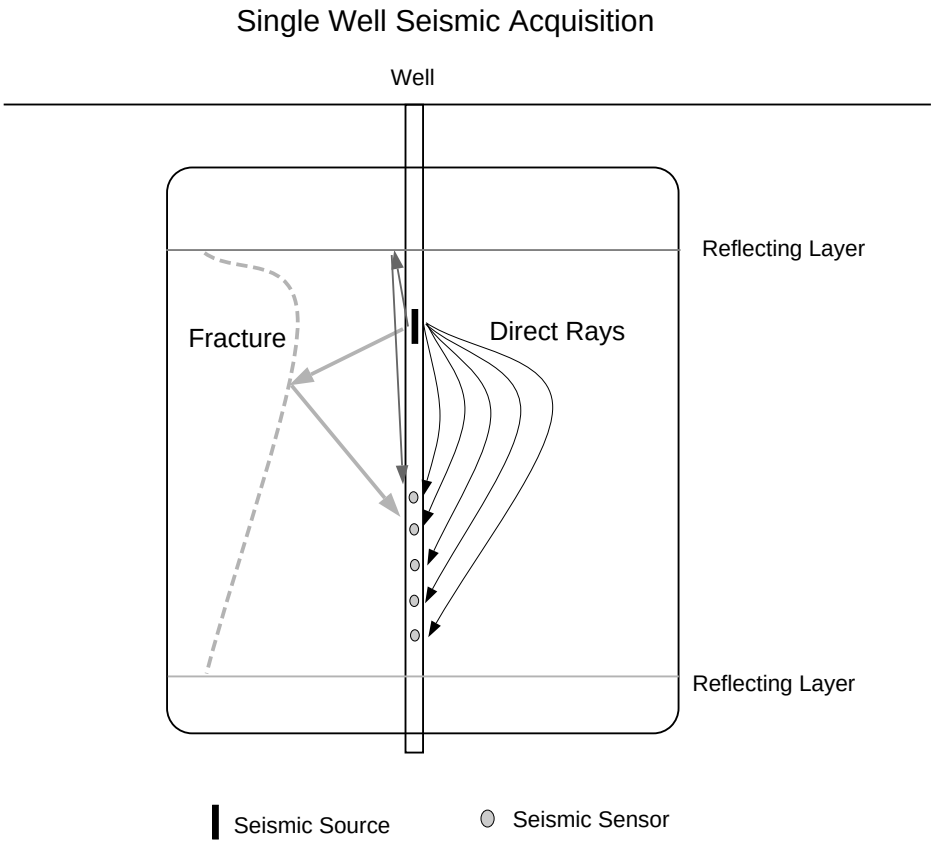

FIG. 12. Wave propagation in single well seismic data acquisition. The sketch displays the principle of wave propagation from the source to the receivers along direct or reflected ray paths.

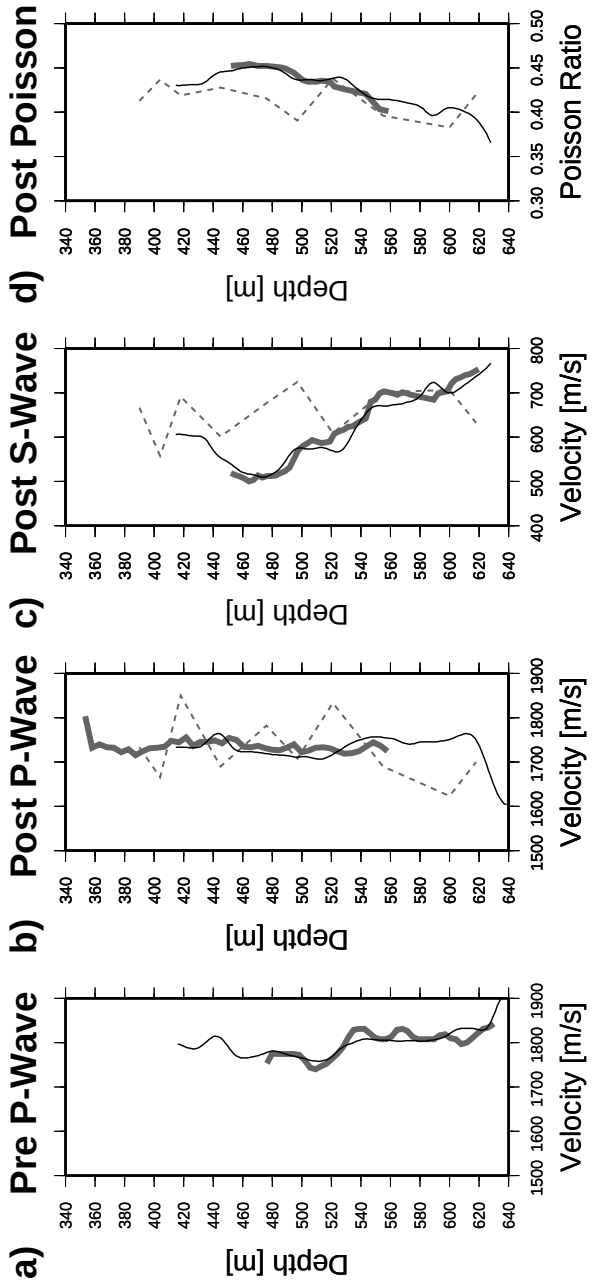

FIG. 13. Comparison between cross well and single well estimates of the velocities and the Poisson ratio. The thin line represents a 5 m horizontal average of estimates along the source borehole from tomographic studies, while the thick line represents the results of the single well study. a) Pre-injection P-wave estimates. b) Post-injection P-wave estimates. c) Post-injection S-wave estimates. d) Post-injection Poisson ratio.

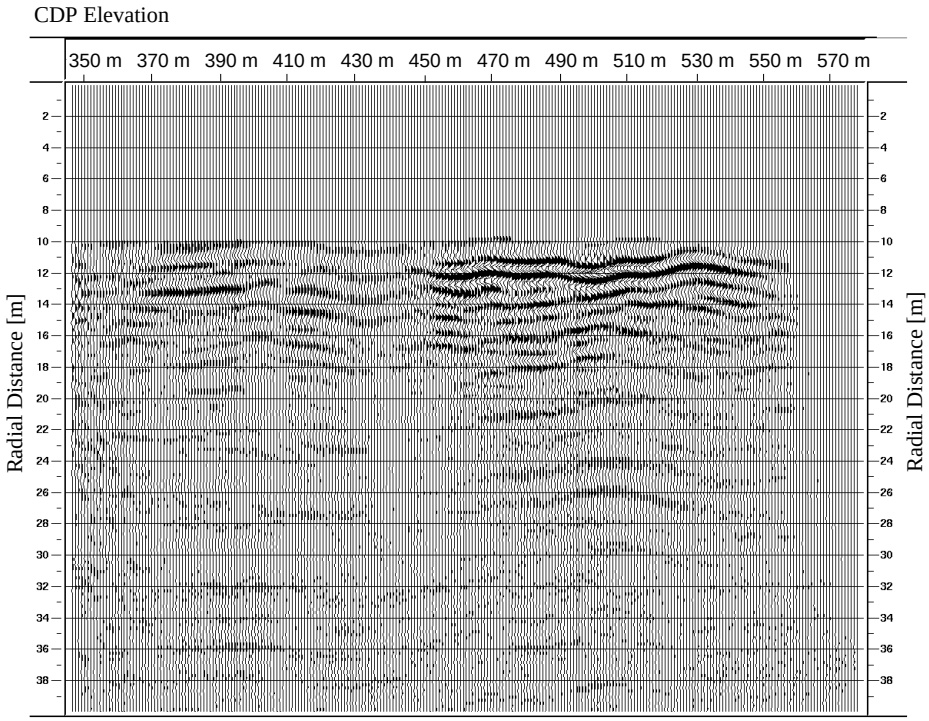

FIG. 14. Results of Kirchoff depth migration using a variable velocity field as estimated from the P-wave travel time inversion. A strong reflection is visible at a radial distance of 10-12 m over a depth interval from 450-550 m while a weaker event is located between a depth of 370-410 m.

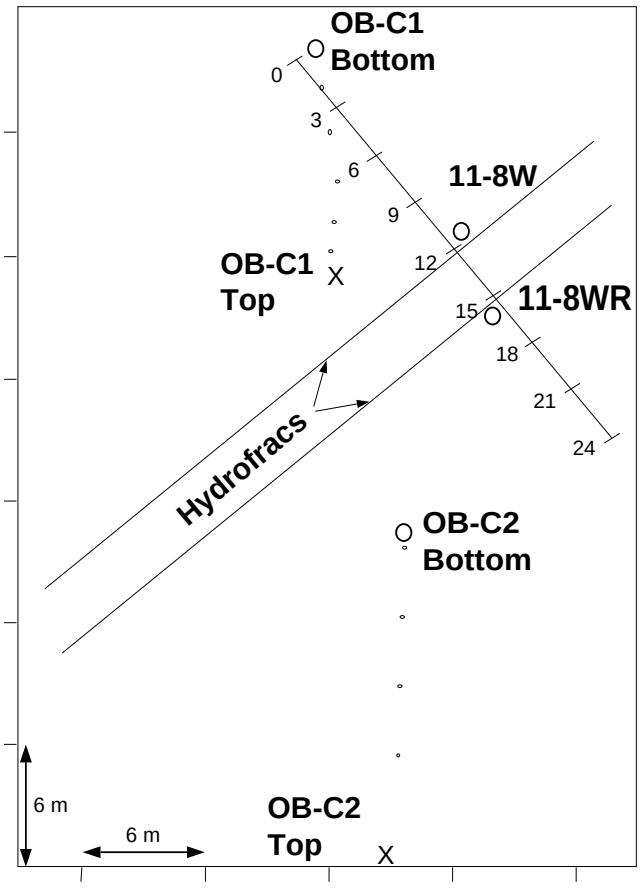

FIG. 15. Geometry of the observation and injection wells. The circles at 12 m and 15 m radial distance from OB-C1 represent respectively, the bottom of 11-8W (the original water injection well) and 11-8WR (the secondary CO_2 injection well which was drilled as a parallel section at the bottom of the orignal borehole 11-8W).